nature geoscience

Article

https://doi.org/10.1038/s41561-025-01703-6

Direct observations of transient weakening during phase transformations in quartz and olivine

Received: 3 June 2024

Accepted: 16 April 2025

Published online: 23 May 2025

Check for updates

Andrew J. Cross[1], Rellie M. Goddard[1,2], Kathryn M. Kumamoto[3], David L. Goldsby[4], Lars N. Hansen[5], Haiyan Chen[6], Diede Hein[5], Christopher A. Thom[7], M. Adaire Nehring[5], Thomas Breithaupt[8] & David Wallis[8]

Phase transformations are widely invoked as a source of rheological weakening during subduction, continental collision, mantle convection and various other geodynamic phenomena. However, despite more than half a century of research, the likelihood and magnitude of such weakening in nature remain poorly constrained. Here we use experiments performed on a synchrotron beamline to reveal transient weakening of up to three orders of magnitude during the polymorphic quartz to coesite (SiO_2) and olivine to ringwoodite (Fe_2SiO_4) phase transitions. Weakening becomes increasingly prominent as the transformation outpaces deformation. We suggest that this behaviour is broadly applicable among silicate minerals undergoing first-order phase transitions and examine the likelihood of weakening due to the olivine-spinel, $(Mg,Fe)_2SiO_4$, transformation during subduction. Modelling suggests that cold, wet slabs are most susceptible to transformational weakening, consistent with geophysical observations of slab stagnation in the mantle transition zone beneath the western Pacific. Our study highlights the importance of incorporating transformational weakening into geodynamic simulations and provides a quantitative basis for doing so.

Rocks and minerals undergo a myriad of solid-state phase transformations during their burial and exhumation through Earth's interior. Such transitions have long been considered a source of mechanical instability[1,2]. For example, rapid changes in volume[3] and elastic properties[4] can generate internal stresses great enough to induce brittle damage, a potential mechanism for nucleating deep-focus earthquakes[3,5]. Phase transitions can also cause rheological (viscous) weakening under conditions that preclude brittle failure. Of particular interest are the phenomena of structural superplasticity and transformation plasticity. Structural superplasticity arises from the formation of fine-grained transformation products that impart long-lived weakening though a transition to grain-size-sensitive creep processes[6,7]. In contrast, transformation plasticity involves only transient weakening during a solid-state phase transformation[8–11], commonly ascribed to enhanced dislocation flux required to accommodate volumetric change[10–12].

Despite their suspected importance, remarkably few studies have examined the rheological impacts of phase transformations in the laboratory. This relative paucity of data largely reflects the technical

---

[1]Department of Geology and Geophysics, Woods Hole Oceanographic Institution, Woods Hole, MA, USA. [2]Department of Geology, Lakehead University, Thunder Bay, ON, Canada. [3]Lawrence Livermore National Laboratory, Livermore, CA, USA. [4]Department of Earth and Environmental Science, University of Pennsylvania, Philadelphia, PA, USA. [5]Department of Earth and Environmental Sciences, University of Minnesota Twin Cities, Minneapolis, MN, USA. [6]Mineral Physics Institute, Stony Brook University, Stony Brook, NY, USA. [7]Rhenium Alloys, North Ridgeville, OH, USA. [8]Department of Earth Sciences, University of Cambridge, Cambridge, UK. ✉e-mail: across@whoi.edu

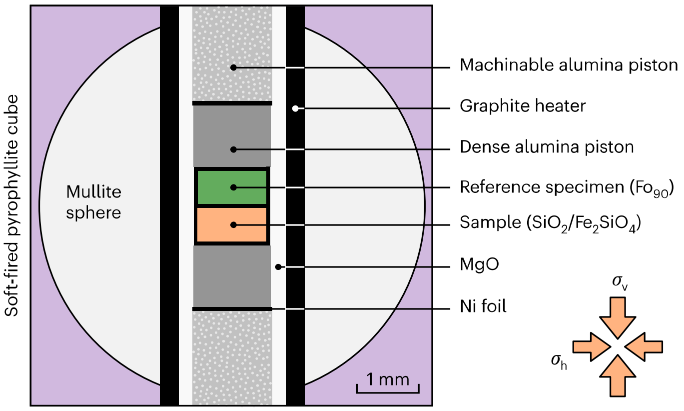

Fig. 1 | Schematic diagram of the D-DIA cell assembly used in this study. Each assembly contained a cylindrical SiO_2 or Fe_2SiO_4 sample stacked in series with a cylindrical Fo_{90} reference specimen, which was used to calculate pressures and bulk stresses via XRD. Heat was generated by passing electrical current through the graphite furnace. Samples were deformed via uniaxial shortening along the vertical axis. σ_v, vertical stress; σ_h, horizontal stress.

challenges associated with resolving transient deformation in situ, particularly at elevated temperatures and pressures. As such, most experimental studies to date have focused on phase transformations that occur at ambient pressure[1,2,13,14] and/or in rock analogues[9,15–17].

To explore the rheological effects of phase transformations at more Earth-relevant conditions, we present experiments performed in a deformation-DIA (D-DIA) apparatus on a synchrotron beamline to examine the quartz↔coesite (SiO_2) phase transition in situ. We chose to focus on SiO_2 for three primary reasons: first, due to its abundance in Earth's crust; second, because the quartz↔coesite transition is readily accessible in the laboratory and third, to treat SiO_2 as a model system for other, more complex silicate minerals. However, to demonstrate the broader applicability of our findings, we also include results from two experiments exploring the olivine↔spinel transformation in Fe_2SiO_4. Iron-rich olivine—fayalite—was chosen because it transforms to its γ-spinel ringwoodite phase—ahrensite—at pressures that are attainable in the D-DIA (7–8 GPa), unlike forsterite (Mg_2SiO_4), which transforms to its β-spinel phase, wadsleyite, at >10 GPa. Furthermore, the transition of olivine directly to ringwoodite may be more directly analogous to the metastable olivine wedge of cold subducting slabs.

We performed two main types of experiment. In hydrostatic control runs, samples were pressurized from the stability field of quartz (or fayalite) to that of coesite (or ahrensite) under isothermal conditions. Confining pressure, differential stress and mineral phase proportions were monitored continuously via energy-dispersive X-ray diffraction (XRD), whereas axial and volumetric strain were measured using X-ray radiography (Methods). After the sample had fully transformed, pressure was lowered to induce the reverse transformation. In non-hydrostatic test runs, the same procedure was followed while simultaneously deforming the sample via uniaxial shortening. Each experimental assembly also contained a fine-grained aggregate of San Carlos olivine, Fo_{90} (Fig. 1), which did not undergo a phase transformation over our range of experimental conditions and was therefore used to consistently calculate the bulk stresses and pressures via XRD. Movies of each experiment are included with the Supplementary Information.

Mechanical evolution during laboratory experiments

Figure 2 shows the typical mechanical evolution of our samples across the quartz↔coesite phase transition. Under hydrostatic conditions, the Fo_{90} reference specimen undergoes a gradual volume reduction of ~4% during pressurization from the quartz to coesite stability fields (Fig. 2g, black triangles). This volume reduction is almost completely reversed during decompression back to the quartz stability field—a small (<1%) residual volumetric strain can be accounted for entirely by elastic effects, considering the difference between the initial and final confining pressures (Fig. 2a). The Fo_{90} volume change is isotropic, such that sample shape remains constant throughout the experiment

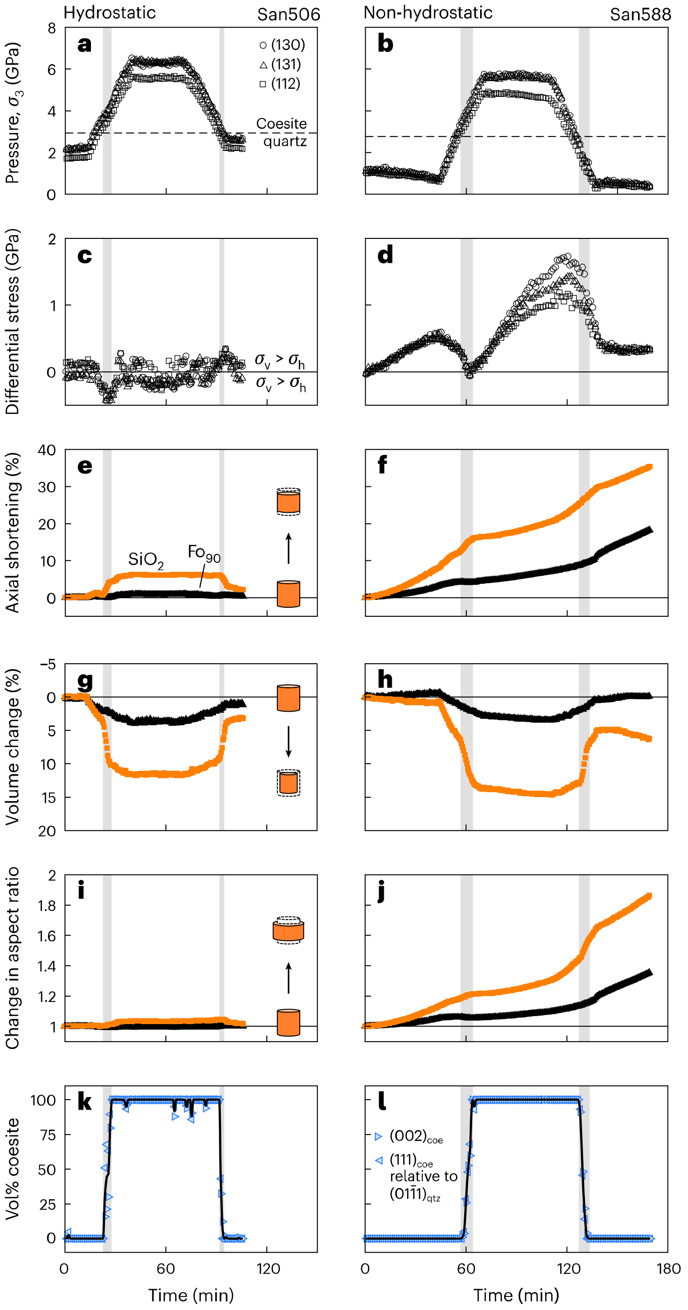

Fig. 2 | Mechanical evolution under hydrostatic and non-hydrostatic conditions. a,**b**, Confining pressure, σ_3. **c**,**d**, Differential stress, $\sigma_v - \sigma_h$. **e**,**f**, Axial strain. **g**,**h**, Volumetric strain. **i**,**j**, Sample aspect ratio (diameter divided by height) normalized relative to the initial sample shape. **k**,**l**, Coesite volume proportion calculated from the relative intensities of quartz and coesite diffraction peaks (Methods), all as functions of time, under hydrostatic (**a**,**c**,**e**,**g**,**i**,**k**) and non-hydrostatic (**b**,**d**,**f**,**h**,**j**,**l**) conditions. The vertical grey bars represent the time intervals over which both quartz and coesite peaks are present in the XRD spectra. The orange squares and black triangles represent the SiO_2 sample and Fo_{90} reference specimen, respectively. Left column shows hydrostatic conditions, and right column shows non-hydrostatic conditions.

https://doi.org/10.1038/s41561-025-01703-6

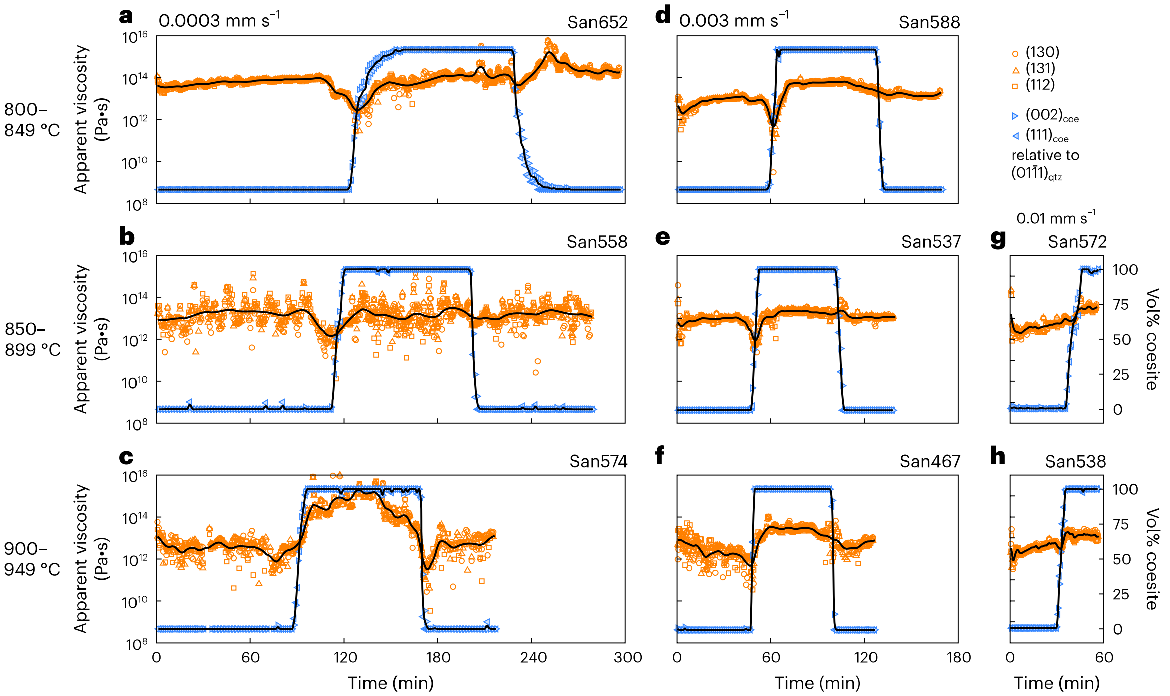

Fig. 3 | Evolution of apparent SiO_2 viscosity as a function of temperature and deformation rate. Experiments were performed under nominalt temperatures of 800–849 °C (**a**,**d**), 850–899 °C (**b**,**e**,**g**), and 900–949 °C (**c**,**f**,**h**), and differential ram rates of 0.0003 mm s^{-1} (**a**,**b**,**c**), 0.003 mm s^{-1} (**d**,**e**,**f**), and 0.01 mm s^{-1} (**g**,**h**). Apparent viscosity (orange symbols) is calculated from the first time-derivative of the SiO_2 axial strain (that is, strain rate) and differential stress from three diffraction peaks in the Fo_{90} reference specimen: (130), (131), and (112). As a visual aid, a spline has been fit through the average of these data (black curve). Also shown (blue symbols) are the volume proportions of coesite as a function of time, calculated from the relative heights of the (002) and (111) XRD peaks in coesite versus the $(01\bar{1}1)$ peak in quartz.

(Fig. 2i). Initially, the SiO_2 sample undergoes a similar gradual volume reduction during pressurization, though more pronounced due to the greater compressibility (that is, smaller bulk modulus) of quartz. However, upon reaching a confining pressure of 3–4 GPa, there is a sharp reduction in volume by ~6% (Fig. 2g, orange squares) coinciding with the emergence of coesite XRD peaks and concomitant loss of quartz XRD peaks (Fig. 2k). During this period, differential stress decreases by 400–500 MPa, placing the sample in deviatoric tension along the vertical axis, or in other words, rotating the maximum principal stress, σ_1, into the horizontal plane (Fig. 2c). Simultaneously, the phase transition introduces a small flattening strain (Fig. 2i) with ~50% of the SiO_2 volume change being accommodated along the vertical axis—greater than the 33% expected for a perfectly isotropic volume change. Nevertheless, this flattening strain is reversed upon passing back through the coesite→quartz phase transition, producing no net change in sample shape and only 2–3% residual axial strain (Fig. 2e) and volumetric strain (Fig. 2g). Again, we largely attribute these residual strains to the difference in confining pressure between the start and end of the experiment.

Under non-hydrostatic conditions, the quartz sample reaches a steady-state strain rate of $3.9 \times 10^{-5}\ s^{-1}$ after ~4% axial shortening, while differential stress continues to increase into the range of several hundred MPa (Fig. 2d). After reaching an axial strain of 8%, we start increasing the confining pressure to induce the quartz→coesite phase transition (Fig. 2b,l). As in the hydrostatic case, the phase transition produces a rapid ~6% volume decrease in the SiO_2 sample (Fig. 2h). Although differential stress decreases gradually during pressurization (due to hysteresis in the D-DIA hydraulic rams; Methods), the quartz→coesite transition itself is accompanied by a rapid and complete relaxation of the differential stress, placing the vertical axis under a deviatoric tensional stress of 50–60 MPa at the mid-point of the phase transition (that is, $\sigma_v < \sigma_h$; Fig. 2d). Differential stress begins increasing thereafter, approaching a steady-state value of 1.0–1.5 GPa in the coesite stability field.

Marked differences between the hydrostatic and non-hydrostatic experiments are observed during depressurization and the associated coesite→quartz transition. Whereas the SiO_2 sample became unflattened during depressurization in the hydrostatic experiment (Fig. 2i), there is considerable additional flattening during the non-hydrostatic coesite→quartz transition (Fig. 2j), despite the increase in sample volume (Fig. 2h). X-ray radiographs reveal that the SiO_2 sample—instead of lengthening, as in the hydrostatic experiment—accommodates the volume increase by expanding within the horizontal plane, perpendicular to σ_1. This observation is common among all of our non-hydrostatic experiments and reflects a 'biasing' (anisotropy) of the volume change in the presence of differential stress, which, in this case, relaxes monotonically by ~1 GPa during the coesite→quartz transition (Fig. 2d). Interestingly, the Fo_{90} sample begins deforming five times faster towards the end of the coesite→quartz transition before returning to a lower strain rate in the quartz stability field (Fig. 2f). Again, this observation is common among our non-hydrostatic experiments and is attributed to internal stresses generated by the SiO_2 volume increase within the deformation assembly—in effect, the SiO_2 sample begins pushing against the Fo_{90} sample as it expands. As shown in Supplementary Fig. 3, remarkably similar behaviour is observed across the fayalite↔ahrensite (Fe_2SiO_4) phase boundary, including the relaxation of differential stress during the up-pressure (fayalite→ahrensite) transformation, and anisotropy of the volume change during the down-pressure (ahrensite→fayalite) transition.

To investigate how deformation conditions influence transient sample strength, we performed non-hydrostatic experiments at nominal temperatures spanning 800–950 °C and differential ram displacement rates corresponding to sample strain rates of 10^{-7}–$10^{-4}\ s^{-1}$ (Extended Data Table 1). Figure 3 shows the apparent viscosity

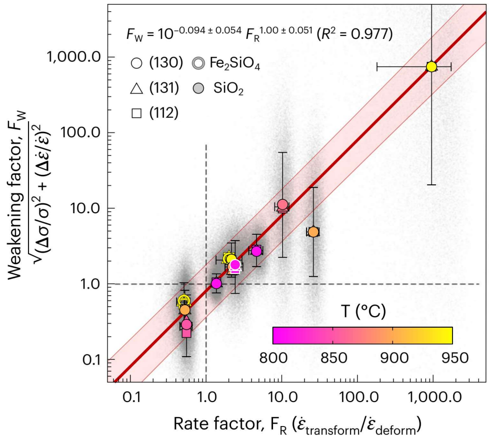

Fig. 4 | Magnitude of transient weakening, F_W, versus the ratio between the transformation and deformation strain rates, F_R. Three weakening factors are calculated for each experiment, one for each Fo_{90} diffraction peak. Data points are coloured according to experiment temperature. Filled symbols represent SiO_2 (quartz→coesite) experiments; open symbols represent Fe_2SiO_4 (fayalite→ahrensite) experiments. The experiment outlined in white (San585) was conducted with a pressure-ramp rate 5–10 times slower than the other experiments. To indicate the experimental uncertainties, we randomly generate 10^4 data points (grey dots) for each experiment based on the uncertainties in F_W and F_R provided in Extended Data Table 1. The error bars correspond to the 1-sigma standard deviations of these 10^4 randomly generated values.

(strength) of our SiO_2 samples as a function of time, alongside the volume proportion of coesite through time. During the quartz→coesite transformation, there is often a dramatic decrease in apparent viscosity centred around the point at which there is a roughly 50–50 vol% mixture of quartz and coesite. Whereas the magnitude of this apparent viscosity decrease is not strongly temperature-dependent—compare, for example, Fig. 3a–c—there is a clear strain-rate dependence. At the lowest deformation rate, the apparent viscosity decreases by 1–2 orders of magnitude during the quartz→coesite transition (Fig. 3a–c), whereas scarcely any viscosity decrease is detected at the highest deformation rate (Fig. 3g–h)—as we discuss below, only a small proportion of this apparent change in viscosity is due to the volumetric contraction (strain-rate increase) and elastic unloading (stress decrease) caused by the transformation. During the reverse, coesite→quartz transformation, there is comparatively little change in apparent viscosity in most experiments. One notable exception is experiment San574, conducted at the highest temperature and lowest strain rate, in which the coesite→quartz transformation produces a more than tenfold reduction in apparent viscosity (Fig. 3c). In this experiment, the sample went into deviatoric tension along the vertical axis ($\sigma_v < \sigma_h$) during the quartz→coesite transformation and back to deviatoric compression ($\sigma_v > \sigma_h$) during the coesite→quartz transformation—the observed apparent viscosity drops reflect these changes in stress state. Even so, given the apparent lack of systematic behaviour for the reverse transformation, we herein focus on the quartz→coesite transition.

Extrapolation to geological timescales

To assess the likelihood and magnitude of transformation-induced weakening under natural conditions, we require a means of extrapolating the observed behaviour to geological timescales. In Fig. 4, we plot the experiments using two dimensionless, scalable parameters: a rate factor and a weakening factor. The rate factor, F_R, represents the ratio between the vertical component of the transient volumetric strain rate and the background (applied) strain rate—for brevity, we refer to these as the transformation and deformation strain rates, $\dot{\varepsilon}_{transform}$ and $\dot{\varepsilon}_{deform}$, respectively—whereas the weakening factor, F_W, represents the combined relative change in differential stress and strain rate (relative to their expected values) during the transformation. Our definition of F_W is somewhat similar to the transformation strain-rate term, $\dot{\gamma}_a$, of Poirier's model for transformation plasticity[10]. Note that we correct F_W to account for the apparent increase in axial strain rate due to the transformation-induced volume decrease (Supplementary Text 2). Whereas the volume decrease also produces elastic unloading of the sample column (that is, a stress drop), we have not removed this effect, as it represents a real, measurable component of the transient viscosity drop—strain rate increases (Fig. 2f) despite the decrease in stress acting on the sample column (Fig. 2d). Nevertheless, as discussed in Supplementary Text 3, elastic unloading accounts for only ~25% of the measured stress drop in our non-hydrostatic experiments. Most of the weakening, we infer, arises from changes to the internal state of the SiO_2 and Fe_2SiO_4 samples during their respective phase transformations.

As shown in Fig. 4, transient weakening, F_W, becomes increasingly pronounced as F_R increases. When the deformation and transformation produce similar axial strain rates (that is, $\dot{\varepsilon}_{transform} \approx \dot{\varepsilon}_{deform}$), very little weakening is observed (for example, San538, San572), whereas the sample becomes up to three orders of magnitude weaker as $\dot{\varepsilon}_{transform}$ exceeds $\dot{\varepsilon}_{deform}$ by approximately three orders of magnitude in our nominally hydrostatic experiment (San506). Figure 4 implies a power-law relationship between F_W and F_R, with >10% weakening occurring ($F_W > 0.1$) once $F_R \gtrsim 0.125$; that is, once $\dot{\varepsilon}_{transform}$ reaches $\gtrsim 1/8$ of $\dot{\varepsilon}_{deform}$. The quartz→coesite ($SiO_2$) and fayalite→ahrensite (Fe_2SiO_4) experiments both obey this relationship within our experimental uncertainty.

To further examine how our observations scale to longer timescales, we performed one experiment where we increased the confining pressure 5–10 times more slowly than in all other experiments (San585; Supplementary Fig. 4, middle column). As with all other non-hydrostatic experiments, the sample experienced a rapid stress decrease (Supplementary Fig. 4e) and transient strain-rate increase (Supplementary Fig. 4h) during the quartz→coesite transformation.

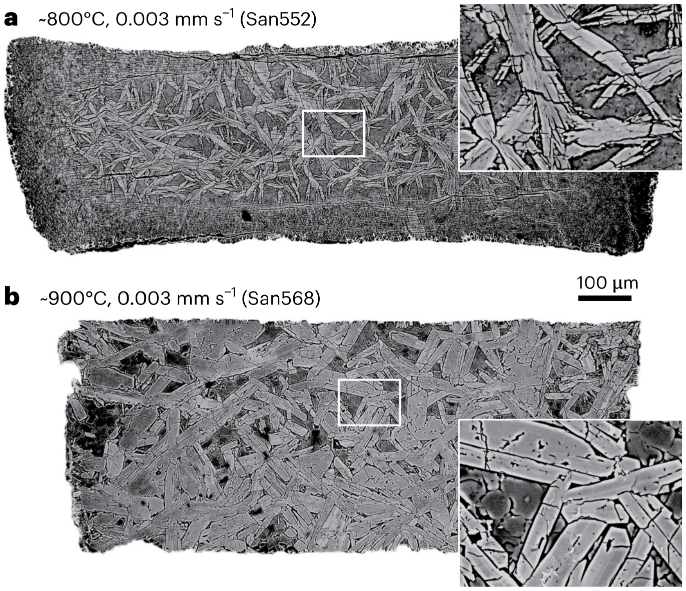

Fig. 5 | Microstructure of samples quenched mid-way through the quartz→coesite phase transformation under non-hydrostatic conditions. Backscattered electron images collected using a Thermo Fisher Helios 5 Hydra scanning electron microscope at the Marine Biological Laboratory, Woods Hole, MA. **a**, Sample from experiment San552, conducted at ~800 °C and 0.003 mm s^{-1} differential ram syringe pump rate (~50% coesite). **b**, Sample from experiment San568, conducted at ~900 °C and also 0.003 mm s^{-1} differential ram syringe pump rate (~90% coesite). The shortening direction is vertical for both samples. The lighter phase is coesite; the darker phase is quartz.

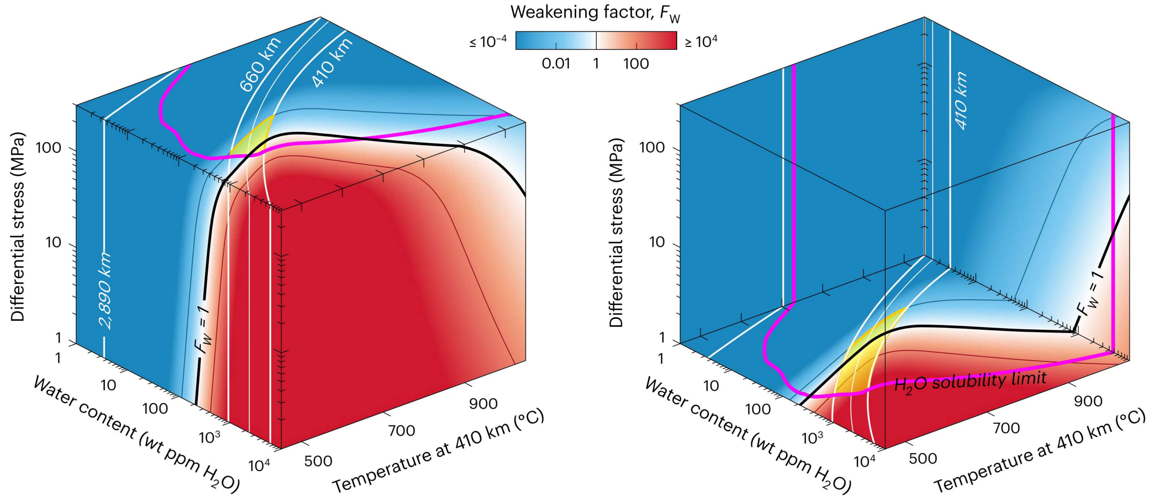

Fig. 6 | Transient weakening factor, F_W, as a function of water content, temperature and differential stress in a subducting slab. White contours indicate the range of conditions over which the maximum transformation rate (that is, the point of maximum weakening) coincides with the mantle transition zone (410–660 km depth). The pink contour indicates the water solubility limit of olivine (Fo_{90})[36], calculated using the Pitzer and Sterner equation of state for H_2O (ref. 37). Conditions that permit slab weakening ($F_W > 0.01$) within the mantle transition zone, and within the solubility limit of Fo_{90}, are highlighted in yellow. Note that each subfigure shows three faces of the cubic parameter space from the same perspective.

The only noteworthy difference is the occurrence of an apparent double viscosity drop (Supplementary Fig. 4q) due to the sample passing twice through the point of zero differential stress: first as the stress state changes from deviatoric compression ($\sigma_v > \sigma_h$) to deviatoric tension ($\sigma_v < \sigma_h$) near the onset of the transformation then back to deviatoric compression upon completion of the transformation (Supplementary Fig. 4e). Crucially, the magnitude of weakening observed in San585 is entirely consistent with our other experiments, plotting on the same trend of F_W versus F_R (symbols outlined in white on Fig. 4).

Microphysical sources of weakening

Previous workers have suggested that phase transitions can produce weakening via transformational faulting[3], grain-size reduction (that is, structural superplasticity)[7] and/or enhanced dislocation motion required to accommodate a transformational volume change (that is, transformation plasticity)[10]. Indeed, similar competitions between applied strain rate and transformation strain rate have also been found in the context of transformational faulting[5,18,19]. Experiments to quantify microstructural evolution across the quartz↔coesite transition are underway and will be presented at a later date. For now, we examine two experimental samples quenched mid-way through the quartz→coesite phase transition: one at ~800 °C (San552) and the other at ~900 °C (San568), both under non-hydrostatic conditions with a displacement rate of 0.003 mm s^{-1}. Backscattered electron images reveal that the samples have undergone 50% and 90% of the transformation to coesite, respectively (Fig. 5). The remnant quartz is equant and fine-grained (1–10 μm diameter at 800 °C, 10–30 μm diameter at 900 °C), similar to the starting material (Methods), whereas coesite presents as large needle- (San552; Fig. 5a) or lath-shaped (San568; Fig. 5b) grains in section, up to 200 μm in length and with aspect ratios frequently >10. Thus, weakening cannot be explained by grain-size reduction in our experiments. There is also no evidence for transformational faulting—only sample San552 contains visible, horizontal cracks, which we attribute to decompression at the end of the experiment. For now, we cannot rule out transformation plasticity. Indeed, our experiments exhibit many features either previously observed or predicted for such behaviour: specifically, anisotropy of the volume change[11] (Fig. 2i,j) and transient weakening that persists only during the phase transition[10] (Fig. 3). However, because transformation plasticity strictly requires the presence of transiently elevated internal stresses and dislocation densities[10–12], we refer to our observed behaviour simply as 'transformation-induced weakening' until detailed microstructural characterization has been completed. This work is currently underway.

Implications for subduction zone dynamics

Having established two scalable parameters, F_R and F_W, we now seek to interrogate whether phase transformations can produce similar weakening under natural conditions. As an example, we consider the case of a slab passing through Earth's mantle transition zone, assuming that our results for SiO_2 and $Fe2SiO_4$ are broadly applicable to first-order phase transformations in other silicates. Following Hosoya et al.[20], we calculate the progression of the olivine-wadsleyite (Mg_2SiO_4) phase transformation for a slab being subducted at a rate of 10 cm yr^{-1}, with a thermal gradient of 0.6 °C kmm s^{-1} and an olivine grain size of 5 mm (Supplementary Fig. 11a). We vary slab temperature at the 410-km discontinuity between 450 °C and 1,050 °C, representing the range of cold to hot subduction zones[21], whereas water content is varied between 1 and 10,000 wt ppm H_2O to encompass dry to water-saturated conditions[22]. The transformation strain rate, $\dot{\varepsilon}_{\text{transform}}$, is taken as one-third of the maximum volumetric strain rate for each set of slab conditions (Supplementary Fig. 11b) assuming an isotropic, 6% total volume reduction based on the densities of olivine and wadsleyite under mantle transition zone pressures. Meanwhile, we calculate slab deformation using rheological flow laws for low-temperature plasticity and wet dislocation creep of olivine[23,24] (Supplementary Fig. 11c) for constant slab stresses of up to 300 MPa (refs. 25–27). The deformation rate, $\dot{\varepsilon}_{\text{deform}}$, is taken as the total strain rate at the same depth as $\dot{\varepsilon}_{\text{transform}}$ for each set of conditions. Weakening, F_W, is then calculated from F_R following the power-law relationship given in Fig. 4. We neglect the role of intracrystalline (martensitic) nucleation for the olivine→spinel transformation, which is thought to proceed more rapidly than intercrystalline (diffusional) nucleation and growth[27]. Thus, our model probably provides a lower bound on F_R (and therefore F_W) by underestimating $\dot{\varepsilon}_{\text{transform}}$. We also neglect the role of secondary phases (for example, pyroxene, garnet), because this is beyond the scope of the present study. However, we speculate that transformation-induced weakening will be more pronounced in polymineralic rocks due to the enhancement of internal stress heterogeneity, as demonstrated by recent numerical models[4]. A detailed description of the model is provided in Supplementary Text 4.

Figure 6 shows the weakening factor, F_W, as a function of water content, temperature and stress in a downgoing slab. Due to the highly nonlinear nature of both the phase transformation kinetics and rheological behaviour, F_W varies over ~30 orders of magnitude, from 10^{-18} to 10^{12} for the range of conditions explored here. Crucially, we find a large swath of parameter space over which $F_W > 0.01$ (that is, $>1\%$)—indicating conditions favourable for transient, transformation-induced weakening of the type seen in our experiments—with more weakening predicted for cold, wet slabs. No appreciable weakening is predicted for slabs in which olivine contains < 10 wt ppm H_2O (or < 70 wt ppm H_2O when slab stresses reach 300 MPa) due to the sluggish transformation kinetics. Furthermore, we find that the point of maximum transient weakening (that is, the depth at which the phase transformation is fastest) coincides with the mantle transition zone (410–660 km depth) for cold, wet slabs (Fig. 6, white contours). These predictions are interesting for two reasons. First, recent water-partitioning experiments have shown that even in wet slabs, olivine will be kinetically dry (containing only ~1 wt ppm H_2O) when coexisting with hydrous phases[22]. Thus, transformational weakening may be triggered by water release upon the thermal breakdown of hydrous phases, with hydration enhancing the olivine transformation kinetics. Second, seismic tomography studies have revealed slabs buckling and stagnating within the mantle transition zone or shallow lower mantle (500–1,000 km depth), particularly along the western margins of the Pacific plate, where old, cold oceanic lithosphere is subducted[28]. Slab stagnation has been ascribed to various phenomena, including heat release during phase transitions[29,30], mantle viscosity structure[31,32], trench retreat[33,34], structural superplasticity[6,7] and transformation plasticity[35]. Our experiments demonstrate that phase transformations can indeed impart dramatic transient weakening, consistent with geophysical observations of slab stagnation in cold, wet slabs. Our results therefore highlight the complex coupling between deformation and metamorphism and provide a quantitative basis for incorporating transformational weakening into geodynamic simulations.

Online content

Any methods, additional references, Nature Portfolio reporting summaries, source data, extended data, supplementary information, acknowledgements, peer review information; details of author contributions and competing interests; and statements of data and code availability are available at https://doi.org/10.1038/s41561-025-01703-6.

References

1. Sauveur, A. What is steel? *Min. Metall.* **5**, 465–468 (1924).
2. Chaklader, A. C. D. Deformation of quartz crystals at the transformation temperature. *Nature* **197**, 791–792 (1963).
3. Green, H. W. II & Burnley, P. C. A new self-organizing mechanism for deep-focus earthquakes. *Nature* **341**, 733–737 (1989).
4. Johnson, S. E., Song, W. J., Cook, A. C., Vel, S. S. & Gerbi, C. C. The quartz $\alpha \leftrightarrow \beta$ phase transition: does it drive damage and reaction in continental crust? *Earth Planet. Sci. Lett.* **553**, 116622 (2021).
5. Gasc, J. et al. Deep-focus earthquakes: from high-temperature experiments to cold slabs. *Geology* **50**, 1018–1022 (2022).
6. Karato, S., Riedel, M. R. & Yuen, D. A. Rheological structure and deformation of subducted slabs in the mantle transition zone: implications for mantle circulation and deep earthquakes. *Phys. Earth Planet. Inter.* **127**, 83–108 (2001).
7. Mohiuddin, A., Karato, S. & Girard, J. Slab weakening during the olivine to ringwoodite transition in the mantle. *Nat. Geosci.* **13**, 170–174 (2020).
8. Gordon, R. B. Observation of crystal plasticity under high pressure with applications to the Earth's mantle. *J. Geophys. Res.* **76**, 1248–1254 (1971).
9. Sammis, C. G. & Dein, J. L. On the possibility of transformational superplasticity in the Earth's mantle. *J. Geophys. Res.* **79**, 2961–2965 (1974).
10. Poirier, J. P. On transformation plasticity. *J. Geophys. Res. Solid Earth* **87**, 6791–6797 (1982).
11. Greenwood, G. W. & Johnson, R. H. The deformation of metals under small stresses during phase transformations. *Proc. R. Soc. Lond. Ser. Math. Phys. Sci.* **283**, 403–422 (1965).
12. Paterson, M. S. Creep in transforming polycrystalline materials. *Mech. Mater.* **2**, 103–109 (1983).
13. Coe, R. S. & Paterson, M. S. The α–β Inversion in quartz: a coherent phase transition under nonhydrostatic stress. *J. Geophys. Res.* **74**, 4921–4948 (1969). *1896-1977*.
14. Gillet, P., Gérard, Y. & Willaime, C. The calcite-aragonite transition: mechanism and microstructures induced by the transformation stresses and strain. *Bull. Minéral.* **110**, 481–496 (1987).
15. Zamora, M. & Poirier, J. P. Experiments in anisothermal transformation plasticity: the case of cobalt. Geophysical implications. *Mech. Mater.* **2**, 193–202 (1983).
16. Zeuch, D. H., Montgomery, S. T. & Keck, J. D. Some observations on the effects of shear stress on a polymorphic transformation in perovskite-structured lead-zirconate-titanate ceramic. *J. Geophys. Res. Solid Earth* **98**, 1901–1911 (1993).
17. Hunt, S. A. et al. Weakening of calcium iridate during its transformation from perovskite to post-perovskite. *Nat. Geosci.* **2**, 794–797 (2009).
18. Burnley, P. C., Green, H. W. & Prior, D. J. Faulting associated with the olivine to spinel transformation in Mg2GeO4 and its implications for deep-focus earthquakes. *J. Geophys. Res.* **96**, 425–443 (1991).
19. Incel, S. et al. Laboratory earthquakes triggered during eclogitization of lawsonite-bearing blueschist. *Earth Planet. Sci. Lett.* **459**, 320–331 (2017).
20. Hosoya, T., Kubo, T., Ohtani, E., Sano, A. & Funakoshi, K. Water controls the fields of metastable olivine in cold subducting slabs. *Geophys. Res. Lett.* **32**, 1–4 (2005).
21. Kirby, S. H., Stein, S., Okal, E. A. & Rubie, D. C. Metastable mantle phase transformations and deep earthquakes in subducting oceanic lithosphere. *Rev. Geophys.* **34**, 261–306 (1996).
22. Ishii, T. & Ohtani, E. Dry metastable olivine and slab deformation in a wet subducting slab. *Nat. Geosci.* **14**, 526–530 (2021).
23. Hirth, G. & Kohlstedt, D. Rheology of the upper mantle and the mantle wedge: a view from the experimentalists. In *Inside the Subduction Factory* (ed. Eiler, J.) Vol. 138, 83–105 (American Geophysical Union, 2003).
24. Warren, J. M. & Hansen, L. N. Ductile deformation of the lithospheric mantle. *Annu. Rev. Earth Planet. Sci.* **51**, 581–609 (2023).
25. Davies, G. F. Mechanics of subducted lithosphere. *J. Geophys. Res. Solid Earth* **85**, 6304–6318 (1980).
26. Bina, C. R. Patterns of deep seismicity reflect buoyancy stresses due to phase transitions. *Geophys. Res. Lett.* **24**, 3301–3304 (1997).
27. Mohiuddin, A. & Karato, S. An experimental study of grain-scale microstructure evolution during the olivine–wadsleyite phase transition under nominally 'dry' conditions. *Earth Planet. Sci. Lett.* **501**, 128–137 (2018).
28. Fukao, Y., Obayashi, M., Nakakuki, T. & the Deep Slab Project Group. Stagnant slab: a review. *Annu. Rev. Earth Planet. Sci.* **37**, 19–46 (2009).
29. Christensen, U. R. & Yuen, D. A. Layered convection induced by phase transitions. *J. Geophys. Res. Solid Earth* **90**, 10291–10300 (1985).
30. Tackley, P. J., Stevenson, D. J., Glatzmaier, G. A. & Schubert, G. Effects of an endothermic phase transition at 670 km depth in a spherical model of convection in the Earth's mantle. *Nature* **361**, 699–704 (1993).

31. Billen, M. I. & Hirth, G. Rheologic controls on slab dynamics. *Geochem. Geophys. Geosyst.* **8**, 1–24 (2007).
32. Čížková, H. & Bina, C. R. Linked influences on slab stagnation: Interplay between lower mantle viscosity structure, phase transitions, and plate coupling. *Earth Planet. Sci. Lett.* **509**, 88–99 (2019).
33. Christensen, U. R. The influence of trench migration on slab penetration into the lower mantle. *Earth Planet. Sci. Lett.* **140**, 27–39 (1996).
34. Yoshioka, S. & Naganoda, A. Effects of trench migration on fall of stagnant slabs into the lower mantle. *Phys. Earth Planet. Inter.* **183**, 321–329 (2010).
35. Panasyuk, S. V. & Hager, B. H. A model of transformational superplasticity in the upper mantle. *Geophys. J. Int.* **133**, 741–755 (1998).
36. Zhao, Y.-H., Ginsberg, S. B. & Kohlstedt, D. L. Solubility of hydrogen in olivine: dependence on temperature and iron content. *Contrib. Mineral. Petrol.* **147**, 155–161 (2004).
37. Pitzer, K. S. & Sterner, S. M. Equations of state valid continuously from zero to extreme pressures for H_2O and CO_2. *J. Chem. Phys.* **101**, 3111–3116 (1994).

Publisher's note Springer Nature remains neutral with regard to jurisdictional claims in published maps and institutional affiliations.

Springer Nature or its licensor (e.g. a society or other partner) holds exclusive rights to this article under a publishing agreement with the author(s) or other rightsholder(s); author self-archiving of the accepted manuscript version of this article is solely governed by the terms of such publishing agreement and applicable law.

© The Author(s), under exclusive licence to Springer Nature Limited 2025

Methods

Starting materials

Dense aggregates of quartz (SiO_2) were prepared via isostatic hot pressing of natural quartz sand with a particle size of 5 µm and >99.5% purity (Min-U-Sil 5, US Silica Corp.). Quartz powders were loaded into a Hot Isostatic Press apparatus at ETH Zurich and hot pressed for 36 h at a temperature of 1,200 °C and gas confining pressure of 200 MPa. No water was added to the powders before hot pressing. After hot pressing, samples were cored to 1.10 ± 0.05 mm diameter and ground to 0.50 ± 0.05 mm height. The mean grain size of the hot-pressed quartz starting material, LT-QHP, was 7.0 ± 3.9 µm, determined using electron backscatter diffraction (EBSD) mapping at the Marine Biological Laboratory (Woods Hole, MA). In two early experimental runs (San467, San468), there was a 4–8% net volume loss within the SiO_2 sample following a two-way traverse of the quartz↔coesite phase boundary, which we attribute to pore collapse in the hot-pressed quartz starting material. In all subsequent experiments, we first cold pressed the sample at room temperature and ~5-GPa confining pressure (to close any pores) before depressurizing to our desired starting pressure of 1–2 GPa. X-ray diffraction (XRD) spectra were collected during some of these cold presses to verify that the SiO_2 sample remained metastable as quartz.

Dense fayalite (Fe_2SiO_4) aggregates were prepared at the University of Minnesota via a similar procedure. First, powders of SiO_2 and Fe_2O_3 were mechanically mixed together before calcining the mixture in a gas-mixing furnace for 50 h at 1,200 °C with oxygen fugacity set to ~10^{-7} Pa. Next, the powders were cold pressed into a Ni capsule, loaded into a Paterson gas-medium apparatus and vacuum hot pressed for 1 h at 1,200–1,250 °C and 300 MPa confining pressure with a vacuum pressure of 10–27 Pa on the interior of the capsule. After hot pressing, samples were cored and ground to 1.10 ± 0.05-mm diameter and 0.50 ± 0.05-mm height. All fayalite samples were extracted from one such hot press, PI-2028. These samples were found to be fully dense and therefore did not need to be further cold pressed in the D-DIA.

Each sample assembly also contained a dense polycrystalline aggregate of hot-pressed San Carlos olivine, Fo_{90} ($(Mg_{0.9}Fe_{0.1})_2SiO_4$), which was primarily used to calculate stress and pressure in situ via energy-dispersive XRD (details provided below). However, the Fo_{90} aggregate also served as a control specimen because forsterite does not undergo any phase transformations over the range of experimental conditions explored here. San Carlos powders with particle size <10 µm containing ~1% orthopyroxene were dried at 1,000 °C for 12 h in a gas-mixing furnace with oxygen before vacuum hot pressing following the same procedure detailed above for fayalite. Fo_{90} reference specimens were extracted from three such hot presses: PI-2056, PI-2094 and PT-1616. We note that the powder used for hot press PI-2094 had a light-grey discolouration, presumably arising from Fe contamination during ball milling—note that Fe contamination should not substantially affect the elastic properties of olivine or, therefore, our stress and pressure measurements. Portions of each hot press were polished using diamond-lapping film down to a grit size of 0.5 µm and finished with a vibratory colloidal silica polish. Polished samples were coated with 5-nm carbon and examined using EBSD at the University of Minnesota on a JEOL JSM 6500 F field emission gun scanning electron microscope operating in high-vacuum mode at an accelerating voltage of 20 kV. EBSD maps were collected at step sizes of 0.5 µm (PI-2056) or 0.1 µm (PI-2094, PT-1616). These maps revealed mean grain sizes (calculated as area-equivalent diameters) of 6.6 ± 3.7 µm, 3.3 ± 1.0 µm and 2.2 ± 1.9 µm for PI-2056, PI-2094 and PT-1616, respectively.

Sample assembly

All experimental assemblies contained one quartz (SiO_2) or fayalite (Fe_2SiO_4) sample stacked in series with one Fo_{90} reference specimen (Fig. 1). Dense alumina and machinable alumina pistons were placed above and below the stacked samples with thin Ni discs separating each component for the purpose of tracking axial strain (that is, sample height) via X-ray radiography. To monitor sample diameter and thereby calculate volumetric strain, the stacked samples were also wrapped in Ni foil. The Ni foil and discs also served to fix oxygen fugacity near the Ni/NiO buffer. The stacked samples and pistons were inserted into a cylindrical MgO sleeve, which itself was contained within a cylindrical graphite resistance heater ('furnace'), a mullite sphere and a soft-fired pyrophyllite cube with edges 6.1–6.35 mm in length (Fig. 1). The mullite sphere and pyrophyllite cube served as pressure media and provided a dry environment for the samples[38], which were not sealed. After assembly, the components were cemented in place with ZrO_2 paste and dried overnight at 100 °C. The assembly did not contain a thermocouple to avoid introducing a source of mechanical instability at high pressure. Instead, temperature was determined using either (1) a calibrated relationship between temperature and furnace power, (2) the flow strength of olivine and/or (3) the kinetics of the quartz→coesite phase transformation. These methods provide minimal loss of accuracy given the inherently large thermal gradients within the small sample assembly[39]. Details on the temperature calibration are provided in Supplementary Text 1.

Apparatus details

Experiments were performed in a Deformation-DIA (D-DIA) apparatus[40] located on beamline sector 6-BM-B of the Advanced Photon Source synchrotron (Argonne National Laboratory). The D-DIA apparatus consists of three orthogonal pairs of anvils sandwiched between an upper and lower guide block, with each anvil in contact with one face of the sample assembly cube. Confining pressure is generated by advancing the main hydraulic ram, which changes the separation distance between the upper and lower guide blocks, advancing the six anvils equally. Meanwhile, deviatoric stress conditions can be imposed by independently moving the vertical pair of anvils, termed 'differential rams'. Differential ram motion is controlled by advancing (or retracting) a pair of hydraulic syringe pumps at a specified rate. Constant syringe pump motion does not perfectly translate into constant strain-rate conditions due to compressibility of the hydraulic fluid. Rather, strain rate evolves to steady state over a period of a few percent strain following each change in experiment conditions (for example, at the start of each experiment or following a phase transformation). Experiment conditions are summarized in Extended Data Table 1.

We note that there is some 'hysteresis' in the hydraulic action of the D-DIA. Specifically, oil pressure in the main (confining) ram appears to evolve more rapidly than pressure in the differential ram. Thus, in our study, σ_h increases more rapidly than σ_v during pressurization (causing differential stress to decrease gradually at the onset of the quartz→coesite pressure ramp; for example, Fig. 2d), whereas σ_h decreases more rapidly than σ_v during depressurization (causing differential stress to increase gradually at the onset of the coesite→quartz pressure ramp; for example, Fig. 2d). However, the axial strain rate of the sample also evolves according to the change in differential stress such that there is minimal change in sample viscosity before the rapid weakening observed at the onset of the phase transition.

In situ stress, strain and phase proportion measurements

Throughout each experiment, synchrotron X-ray radiation was used to calculate stress, pressure and quartz-coesite (or fayalite-ahrensite) volume proportions via energy-dispersive XRD and axial and volumetric strain via X-ray radiography. The detector geometry and procedures for calculating stress and strain have been described in detail elsewhere[39,41–43]. In short, XRD data were obtained by directing a 100 × 100 µm white (polychromatic) X-ray beam through a gap between the upstream horizontal anvils into the sample assembly. Diffraction spectra were collected at a downstream array of ten solid-state detectors arranged at fixed azimuths of $\Psi = 0–270°$ with respect to the horizontal incident beam[39]. The detectors, along with a set of conical slits, were positioned such that the X-ray beam was collimated to a Bragg angle of $2\theta \approx 6.5°$. The precise Bragg angle was calibrated approximately once every three experiments (that is, once per day) using a powdered Al_2O_3 standard. Each XRD energy peak corresponds to a (**hkl**) plane for which the lattice spacing, $d_{\mathbf{hkl}}$, is obtained using Bragg's law. Changes in d-spacing under load (that is, lattice strain) provide quantitative constraints on the stress state of a sample via its elastic properties. During uniaxial shortening in the D-DIA, lattice strain should be greatest in the (horizontal) plane normal to the shortening axis and least in any (vertical) plane containing the shortening axis. Thus, differential stress is given by the difference in $d_{\mathbf{hkl}}$ at $\Psi = 0°$ and $\Psi = 90°$ via the Singh et al.[44] formulation of Hooke's law, which assumes an isostress condition.

Diffraction patterns were alternately collected between the sample and Fo_{90} reference specimen with dwell times of 5–30 s. We calculated stresses and pressures using only the Fo_{90} XRD data, assuming the stress states in the stacked samples to be the same—previous workers have shown this to be a reasonable assumption within experimental uncertainty[42,43,45]. This approach was chosen because Fo_{90} produces several strong XRD peaks that can be used for stress calculation (Supplementary Fig. 1), its elasticity is well characterized and it does not undergo a phase transformation over the range of experimental conditions explored here so serves as a reliable and continuous reference specimen. Here stress and pressure were calculated using the (130), (131) and (112) Fo_{90} diffraction peaks, along with the elastic constants for San Carlos olivine from Abramson et al.[46], their pressure derivatives[46] and their temperature derivatives[47]. Mean stress was calculated using a third-order Birch–Murnaghan equation of state for olivine, with values of 129.4 GPa and 4.29 for the Fo_{90} bulk modulus and its pressure derivative, respectively[46], −0.02 GPa K^{-1} for the temperature derivative of the bulk modulus[48] and the thermal expansivity of olivine from Suzuki[49]. Note that we draw a distinction between confining pressure, $P_c = \sigma_3$ and mean stress, $\sigma_m = (\sigma_1 + 2\sigma_3)/3$, wherein we assume that $\sigma_2 = \sigma_3$, given the axisymmetric deformation geometry.

In many experimental runs, σ_1 rotates from the vertical axis (parallel with the applied shortening direction) into the horizontal plane (perpendicular to the applied shortening direction) during the quartz↔coesite and fayalite↔ahrensite phase transitions. Thus, to provide a consistent reference frame, we calculate differential stress as $\sigma_d = \sigma_v - \sigma_h$ (rather than $\sigma_d = \sigma_1 - \sigma_3$), where σ_v and σ_h represent stress along the vertical (shortening) axis and in the horizontal plane, respectively. Positive values indicate deviatoric compression along the vertical axis (that is, $\sigma_v > \sigma_h$), whereas negative values indicate deviatoric tension along the vertical axis (that is, $\sigma_v > \sigma_h$). In other words, $\sigma_d > 0$ indicates $\sigma_1 \parallel \sigma_v$, whereas $\sigma_d < 0$ indicates $\sigma_1 \parallel \sigma_h$.

Due to the plastic anisotropy of olivine, there is some variation in stress measured using the different lattice planes, typically on the order of 50–200 MPa at any given point. Previous experimental studies have suggested that the olivine peak that produces the greatest stress estimate—typically (130), in our study—provides the most accurate measure of the bulk stress for olivine aggregates in compression[43,45].

SiO_2 and Fe_2SiO_4 diffraction patterns were used to monitor the quartz-coesite and fayalite-ahrensite phase proportions, respectively. Volume proportions were calculated using the relative intensities (heights) of peaks belonging to the low-pressure (quartz, fayalite) or high-pressure (coesite, ahrensite) phases. As many of the diffraction peaks in quartz and coesite, and fayalite and ahrensite, are overlapping, we limited our analysis to the $(01\bar{1}1)$ peak in quartz, the (002) and (111) peaks in coesite, the (130) peak in fayalite and the (220) and (331) peaks in ahrensite (Supplementary Fig. 1). Peaks were tracked in each of the ten detectors separately, following the subtraction of any background (long wavelength) intensity variation. To account for detector-to-detector variations in signal intensity, each spectrum was also normalized to the range 0–1. Phase volume proportions were calculated for each combination of peaks as follows:

$$X_{\mathrm{B}} \equiv 1 - X_{\mathrm{A}} = \frac{I_{\mathrm{B}\mathbf{hkl}}}{(I_{\mathrm{B}\mathbf{hkl}} + I_{\mathrm{A}\mathbf{hkl}})}$$

where X is mineral volume fraction and I is the mean normalized intensity of a particular (**hkl**) peak across all ten detectors, divided by the maximum expected intensity of that (**hkl**) peak from X-ray powder diffraction (Supplementary Fig. 1). The subscripts 'A' and 'B' denote the low-pressure (quartz, fayalite) and high-pressure (coesite, ahrensite) phases, respectively. In practice, the minimum detectable amount of either phase is ~0.75%. Furthermore, the four peak combinations—$(01\bar{1}1)_{qtz}$ versus $(002)_{coe}$, $(01\bar{1}1)_{qtz}$ versus $(111)_{coe}$, $(130)_{fay}$ versus $(220)_{ahr}$ and $(130)_{fay}$ versus $(331)_{ahr}$—give estimates within 10% of one another at the 2-sigma level in all experiments. These sensitivities could be improved by collecting diffraction patterns over longer dwell times; however, we favoured short dwell times to provide better temporal resolution during the phase transformations. We should also note that the XRD patterns represent only a 100 × 100 × 1,000 µm volume within the centre of our samples, corresponding to ~2.5% of the total sample volume. As such, the measured phase proportions may not be fully representative of the entire sample volume, particularly if the phase transformation is heterogeneous (for example, due to the heterogeneity of nucleation sites or thermal gradients within the sample). Indeed, sample volume typically evolves over a longer transient period during a phase transformation than the XRD patterns alone would indicate. Nevertheless, the estimated onset and end of the phase transformation typically correspond very closely to the times at which rapid changes in strain rate are observed (for example, Fig. 2g–h).

Finally, axial and volumetric strains were calculated via digital image cross-correlation of X-ray radiographs collected at 5–30-s intervals throughout each experiment with 1,024 × 1,360 pixel resolution. Interpolation of the X-ray intensity data enabled sub-pixel resolution when tracking the movement of the Ni foils, yielding axial strain resolution down to 10^{-5} and volumetric strain resolution down to 10^{-4}. Volumetric strains were calculated from the two-dimensional X-ray radiographs assuming a cylindrical sample shape and cylindrical symmetry around the compression (vertical) axis. Radiographs were taken of the sample in orthogonal orientations after every experimental run and used to confirm that cylindrical symmetry was indeed maintained. We estimate that our volumetric strain measurements are generally accurate to within ± 1% except in cases where the sample deviates substantially from cylindricity due to, for example, high-strain deformation (Supplementary Fig. 2), which produces a gradual apparent 'increase' in volumetric strain (that is, volume 'loss') during non-hydrostatic experiments conducted to high strains (for example, Fig. 2h). Even so, our volumetric strain measurements remain accurate to within < 6%, producing very little impact on the calculated volumetric strain rates and transformation rates. For example, the volumetric strain-rate uncertainty for San588 (Fig. 2h) is ~5×10^{-6} s^{-1}—roughly 2% of the measured value—assuming, for simplicity, that the volumetric strain uncertainty increases linearly through time (meaning that only ~0.1% volumetric strain uncertainty accumulates during the quartz↔coesite phase transition).

Axial and volumetric strains are mostly presented here as engineering strains; however, we calculate strain rate and viscosity using true (logarithmic) strains. Shortening strains are reported as positive, whereas extensional strains are reported as negative. Following a similar convention, sample contraction (that is, volume decrease) is reported as a positive volumetric strain, whereas sample expansion (that is, volume increase) is reported as a negative volumetric strain.

Experiment procedure

In each SiO_2 experiment, samples were pressurized to 1–2 GPa confining pressure with the differential rams fully retracted (following the ~5 GPa cold press described above). Fe_2SiO_4 experiments were pressurized to ~4 GPa initial pressure (without a ~5 GPa cold press). Pressurization typically introduced some differential stress (< 500 MPa), which we relaxed by annealing the samples for 10–30 min at 209 W (nominally 800–900 °C). XRD patterns were monitored throughout the anneal to verify (1) that the differential stresses became fully relaxed and (2) that the samples remained within their respective low-pressure stability fields. The differential rams were then advanced (at the syringe pump rates listed in Extended Data Table 1) to begin deforming the sample and Fo_{90} reference specimen via uniaxial shortening. Once deformation had reached a steady state (with the exception of San574, which even after 11% axial strain did not reach steady state), the main ram was steadily advanced to begin increasing the confining pressure. In most experiments, hydraulic load on the main ram was increased at a rate of 0.018–0.037 tons per second, corresponding to a pressure-ramp rate of 2–5 MPa s^{-1} (Extended Data Table 1). However, one experiment (San585) was pressurized at ~0.5 MPa s^{-1}.

Upon reaching the high-pressure stability field, we waited for the quartz→coesite or fayalite→ahrensite transformation to reach completion and for deformation of the sample and Fo_{90} reference specimen to reach a new steady state before reducing pressure to return to the low-pressure stability field. Note that in both SiO_2 runs performed at our highest deformation rate—0.01 mm s^{-1} (San538, San572)—we stopped the experiments in the coesite stability field to avoid the D-DIA anvils coming into contact due to the large shortening strains reached. In all other experiments, we again waited for the reverse transformation to reach completion and for deformation of the sample and Fo_{90} specimen to reach steady state, before stopping the experiment. Each experiment was stopped by cutting power to the graphite furnace and stopping the differential rams in quick succession. The load on the main ram was then removed to depressurize the assembly, keeping the differential rams in their advanced position to maintain a small positive deviatoric stress on the sample and thereby minimize decompression cracking.

Data availability

The stress, strain and phase proportion measurements for each experimental run provided in Supplementary Data 1 and Supplementary Videos 1–14 are also publicly available via Figshare at https://doi.org/10.6084/m9.figshare.28726712 (ref. 50).

Code availability

The MATLAB code used for the slab weakening model is provided in Supplementary Code 1 and is also publicly available via Figshare at https://doi.org/10.6084/m9.figshare.28726712 (ref. 50).

References

38. Durham, W. B., Mei, S., Kohlstedt, D. L., Wang, L. & Dixon, N. A. New measurements of activation volume in olivine under anhydrous conditions. *Phys. Earth Planet. Inter.* **172**, 67–73 (2009).
39. Dixon, N. A. & Durham, W. B. Measurement of activation volume for creep of dry olivine at upper-mantle conditions. *J. Geophys. Res. Solid Earth* **123**, 8459–8473 (2018).
40. Wang, Y., Durham, W. B., Getting, I. C. & Weidner, D. J. The deformation-DIA: a new apparatus for high temperature triaxial deformation to pressures up to 15 GPa. *Rev. Sci. Instrum.* **74**, 3002–3011 (2003).
41. Weidner, D. J. et al. Precise stress measurements with white synchrotron X rays. *Rev. Sci. Instrum.* **81**, 013903 (2010).
42. Hansen, L. N. et al. Low-temperature plasticity in olivine: grain size, strain hardening, and the strength of the lithosphere. *J. Geophys. Res. Solid Earth* **124**, 5427–5449 (2019).
43. Goddard, R. M. et al. Validation of subgrain-size piezometry as a tool for measuring stress in polymineralic rocks. *ESS Open Archive* https://doi.org/10.22541/essoar.169755254.46171679/v1 (2023).
44. Singh, A. K., Balasingh, C., Mao, H., Hemley, R. J. & Shu, J. Analysis of lattice strains measured under nonhydrostatic pressure. *J. Appl. Phys.* **83**, 7567–7575 (1998).
45. Girard, J., Silber, R. E., Mohiuddin, A., Chen, H. & Karato, S. Development of a stress sensor for in-situ high-pressure deformation experiments using radial X-ray diffraction. *Minerals* **10**, 166 (2020).
46. Abramson, E. H., Brown, J. M., Slutsky, L. J. & Zaug, J. The elastic constants of San Carlos olivine to 17 GPa. *J. Geophys. Res. Solid Earth* **102**, 12253–12263 (1997).
47. Isaak, D. G. High-temperature elasticity of iron-bearing olivines. *J. Geophys. Res. Solid Earth* **97**, 1871–1885 (1992).
48. Mao, Z. et al. Elasticity of single-crystal olivine at high pressures and temperatures. *Earth Planet. Sci. Lett.* **426**, 204–215 (2015).
49. Suzuki, I. Thermal expansion of periclase and olivine, and their anharmonic properties. *J. Phys. Earth* **23**, 145–159 (1975).
50. Cross, A. J. et al. Supplementary data for 'direct observations of transient weakening during phase transformations in quartz and olivine'. *Figshare* https://doi.org/10.6084/m9.figshare.28726712 (2025).

Acknowledgements

We thank L. Tokle and A. Dillman for providing the quartz and olivine starting materials, respectively. This work was funded through National Science Foundation (NSF) awards EAR-2023128 (to A.J.C.), EAR-2003389 (to A.J.C.), EAR-2023058 (to D.L.G.), EAR-2023061 (to L.N.H.) and EAR-1806791 (to K.M.K.). D.W. was supported by a UK Research and Innovation Future Leaders Fellowship, MR/V021788/1. A.J.C. acknowledges additional salary support from the Investment in Science Program (ISP) and Assistant Scientist Endowment Support (ASES) programmes at Woods Hole Oceanographic Institution (WHOI). Use of the Advanced Photon Source, Argonne National Laboratory, was supported by the US Department of Energy, Office of Science, Office of Basic Energy Sciences, under contract number DE-AC02-06CH11357. Use of the 6-BM-B beamline was supported by COMPRES, the Consortium for Materials Properties Research in Earth Sciences, under NSF Cooperative Agreement EAR 16-06856. Portions of this work were performed under the auspices of the US Department of Energy by Lawrence Livermore National Laboratory under contract DE-AC52-07NA27344. LLNL-JRNL-859365.

Author contributions

A.J.C. and D.L.G. conceived of the study. All authors helped to conduct the experiments. K.M.K., L.N.H. and A.J.C. wrote the code for processing the experiment data. A.J.C. performed all the data processing, analysis and modelling. A.J.C. wrote the paper, with review and editing provided by all authors.

Competing interests

The authors declare no competing interests.

Additional information

Extended data is available for this paper at https://doi.org/10.1038/s41561-025-01703-6.

Supplementary information The online version contains supplementary material available at https://doi.org/10.1038/s41561-025-01703-6.

Correspondence and requests for materials should be addressed to Andrew J. Cross.

Peer review information *Nature Geoscience* thanks Julien Gasc and the other, anonymous, reviewer(s) for their contribution to the peer review of this work. Primary Handling Editor: Alison Hunt, in collaboration with the *Nature Geoscience* team.

Reprints and permissions information is available at www.nature.com/reprints.

Extended Data Table 1 | Experiment run conditions

Experiment #	Sample	Fo$_{90}$ reference specimen	Graphite furnace origin	Furnace power (W)	Temp. (°C)	Diff. ram syringe pump rate (mm/s)	Pressure ramp rate, up / down (MPa/s)	Rate factor, F_R	Log$_{10}$ weakening factor, F_W		
									(112) peak	(131) peak	(130) peak
San467[a]	Quartz	PI-2056	Oxford	209	944[b]	0.003	4.6 / 3.6	2.2 ± 0.81	0.32 ± 0.23	0.30 ± 0.21	0.32 ± 0.22
San471[a]	Fayalite	PI-2056	Oxford	209	945[b]	0.01	2.8 / 3.1	0.51 ± 0.10	−0.26 ± 0.26	−0.23 ± 0.25	−0.22 ± 0.24
San506	Quartz	PI-2056	Oxford	189	945[b]	0	2.6 / 2.6	950 ± 770	2.9 ± 1.6	2.9 ± 1.6	2.9 ± 1.6
San537	Quartz	PI-2056	Oxford	167	892[b]	0.003	2.6 / 2.9	2.2 ± 0.18	0.18 ± 0.048	0.17 ± 0.042	0.23 ± 0.018
San538	Quartz	PI-2056	Oxford	167	903[b]	0.01	3.1 / N/A	0.53 ± 0.042	−0.34 ± 0.24	−0.35 ± 0.23	−0.34 ± 0.26
San540[a]	Fayalite	PI-2056	Oxford	230	957[b]	0.003	2.7 / 3.2	2.0 ± 0.31	0.34 ± 0.059	0.33 ± 0.067	0.33 ± 0.056
San558	Quartz	PI-2094	Oxford	167	869[b]	0.0003	2.8 / 3.3	10 ± 2.2	1.0 ± 0.60	1.0 ± 0.66	1.1 ± 0.69
San572	Quartz	PI-2094	Oxford	198	851[b]	0.01	2.5 / N/A	0.55 ± 0.10	−0.65 ± 0.31	−0.50 ± 0.35	−0.54 ± 0.38
San574	Quartz	PI-2094	Oxford	209	901[b]	0.0003	2.6 / 2.4	26 ± 4.9	0.69 ± 0.59	0.69 ± 0.59	0.69 ± 0.59
San585	Quartz	PT-1616	UMN	209	810[c]	0.0004	0.41 / 0.60	2.4 ± 0.64	0.20 ± 0.32	0.22 ± 0.32	0.25 ± 0.32
San588	Quartz	PT-1616	UMN	209	810[c]	0.0003	3.1 / 3.2	1.4 ± 0.16	0.021 ± 0.11	0.0068 ± 0.13	0.0041 ± 0.12
San652	Quartz	PT-1616	UMN	209	810[c]	0.003	2.4 / 2.2	4.6 ± 0.98	0.45 ± 0.20	0.44 ± 0.20	0.43 ± 0.20
Mid-transformation quench											
San552	Quartz	PI-2094	Oxford	209	807[b]	0.003	1.3 / N/A	–	–	–	–
San568	Quartz	PI-2094	Oxford	209	900[b]	0.003	2.9 / N/A	–	–	–	–

[a] Experiment performed without initial room-temperature pressure cycle (see Methods for details) [b] Temperature inferred from the quartz→coesite transformation kinetics and/or olivine flow strength (see Methods for details). ± 60 °C uncertainty. [c] Temperature calculated using power-temperature calibration (Supplementary Fig. 4; Supplementary Eq. 1). ± 20 °C uncertainty.